EMBRY-RIDDLE
Aeronautical University™
SCHOLARLY COMMONS

Physical Sciences - Daytona Beach

College of Arts & Sciences

1-29-2005

Maui Mesosphere and Lower Thermosphere (Maui MALT) Observations of the Evolution of Kelvin-Helmholtz Billows Formed Near 86 km Altitude

J. H. Hecht
Aerospace Corporation

Alan Z. Liu
Embry Riddle Aeronautical University - Daytona Beach, liuz2@erau.edu

R. L. Walterscheid
Aerospace Corporation

R. J. Rudy
Aerospace Corporation

Follow this and additional works at: https://commons.erau.edu/db-physical-sciences

Part of the Physical Sciences and Mathematics Commons

Scholarly Commons Citation

Maui Mesosphere and Lower Thermosphere (Maui MALT) observations of the evolution of Kelvin-Helmholtz billows formed near 86 km altitude

J. H. Hecht

Space Science Applications Laboratory, Aerospace Corporation, Los Angeles, California, USA

A. Z. Liu

Department of Electrical and Computer Engineering, University of Illinois, Urbana, Illinois, USA

R. L. Walterscheid and R. J. Rudy

Space Science Applications Laboratory, Aerospace Corporation, Los Angeles, California, USA

[1] Small-scale (less than 15 km horizontal wavelength) structures known as ripples have been seen in OH airglow images for nearly 30 years. The structures have been attributed to either convective or dynamical instabilities; the latter are mainly due to large wind shears, while the former are produced by superadiabatic temperature gradients. Dynamical instabilities produce Kelvin-Helmholtz (KH) billows, which have been known for many years. However, models and laboratory experiments suggest that these billows often spawn a secondary instability that is convective in nature. While laboratory investigations see evidence of such structures, the evolution of these instabilities in the atmosphere has not been well documented. The Maui Mesosphere and Lower Thermosphere (Maui MALT) Observatory, located on Mt. Haleakala, is instrumented with a Na wind/temperature lidar that can detect dynamic or convective instabilities with 1 km vertical resolution over the altitude region from about 85 to 100 km. The observatory also includes a fast OH airglow camera, sensitive to emissions coming from approximately 82 to 92 km altitude, which obtains images every 3 s at sufficient resolution and signal to noise to see the ripples. On 15 July 2002, ripples were observed moving at an angle to their phase fronts. After a few minutes, structures appeared to form approximately perpendicular to the main ripple phase fronts. The lidar data showed that a region of dynamical instability existed from approximately 85.5 to 87 km and that the direction of the wind shear in this region was consistent with the phase fronts of the ripple features. The motion of the ripples themselves was consistent with the wind velocity at 85.9 km. Thus in this case the observed ripple motion was the advection of KH billows by the wind. The perpendicular structures were seen to be associated with the KH billows: they formed at the time when the atmosphere briefly became convectively unstable within the region where the KH billows most likely formed. Because of this and because the ripples were oriented approximately perpendicular to and moved with the billows, we speculate that they are the secondary instabilities predicted by models of KH evolution. The primary and perpendicular features were seen to decay into unstructured regions suggestive of turbulence. While the formation and decay time appear consistent with models, the horizontal wavelength of the perpendicular structures seems to be larger than models predict for the secondary instability features.

Citation: Hecht, J. H., A. Z. Liu, R. L. Walterscheid, and R. J. Rudy (2005), Maui Mesosphere and Lower Thermosphere (Maui MALT) observations of the evolution of Kelvin-Helmholtz billows formed near 86 km altitude, *J. Geophys. Res.*, *110*, D09S10, doi:10.1029/2003JD003908.

1. Introduction

[2] Since the first mesopause region airglow imaging observations about 30 years ago [*Peterson and Kieffaber,*

1973], most of the structures seen have been attributed to the passage of atmospheric gravity waves (AGWs) that are generated in the troposphere and propagate upward to the upper mesosphere and lower thermosphere [e.g., *Moreels and Herse*, 1977; *Hecht et al.*, 1995; *Swenson et al.*, 1995; *Taylor et al.*, 1995; *Nakamura et al.*, 1999; *Smith et al.*, 2000]. Recent studies suggest that some of these AGWs may be ducted a considerable distance from their source [e.g., *Walterscheid et al.*, 1999; *Hecht et al.*, 2001a]. Passage of these waves through the airglow emission layer in the mesopause perturbs the neutral density and temperature, which subsequently perturbs the airglow emission. Images of the airglow when AGWs pass through show bright and dark regions that, when seen in a time sequence, appear as a series of wave-like structures moving across the sky.

[3] There are, however, structures seen in airglow images that are more likely generated by instabilities in the emission line layer itself. These features termed ''ripples'' have been the subject of much study by several investigators [e.g., *Peterson*, 1979; *Taylor and Hapgood*, 1990; *Taylor and Hill*, 1991; *Taylor et al.*, 1997; *Hecht et al.*, 1997, 2000]. By making simultaneous observations with airglow imagers and with either Na wind/temperature lidars or with medium-frequency (MF) radars, both superadiabatic lapse rates and large wind shears have been shown to cause some of these structures [*Hecht et al.*, 1997, 2000, 2001b]. Structures that form in unstable regions resulting from large wind shears are known as Kelvin-Helmholtz (KH) billows. Over 30 years ago they were reported in chemical release rocket experiments and in noctilucent cloud displays [e.g., *Hauritz*, 1964; *Lloyd et al.*, 1973]. In principle, the combination of airglow observations and Na lidar wind/temperature data provides a new means of studying the physics of the evolution of KH features.

[4] KH instability features have been known for over 100 years, and a recent paper by *Fritts et al.* [1996] cites many of the important papers published to date on this phenomenon. The basic model applicable to the atmosphere is that when the ratio of the static stability to the square of the wind shear is low (less than 0.25), the atmosphere becomes dynamically unstable and a region of Kelvin-Helmholtz billows forms [e.g., *Chandrasekhar*, 1981; *Miles and Howard*, 1964; *Scorer*, 1969; *Gossard and Hooke*, 1975]. Many of the billow features such as horizontal wavelength and height depend on the vertical extent of the unstable region. The lifetime and evolution of these billows and their subsequent dissipation and formation of turbulence, however, are far less understood [e.g., *Fritts et al.*, 1996]. It is the mixing of atmospheric species by the formation of KH billows and the resulting turbulence that are important in understanding the structure of the atmosphere in the upper mesosphere and lower thermosphere.

[5] The visual evolution of KH features have been studied both observationally and theoretically. Laboratory studies pioneered by *Thorpe* [1968] suggested that as KH billows evolve, secondary instabilities form that precede the decay into turbulence [e.g., *Thorpe* 1973]. The existence of these secondary structures, which were predicted to be convectively unstable, was anticipated by observations in the ocean [*Woods*, 1969] and by modeling [*Orlanski and Bryan*,

1969]. Observations of KH billow formation have also been made in the lower atmosphere [e.g., *Browning and Watkins*, 1970; *Browning*, 1971]. However, some laboratory observations have been hampered by wall effects [*Thorpe*, 1985, 1987], and it has not been confirmed that the same evolution of the KH primary and secondary instabilities observed in such experiments actually occurs in the atmosphere. The physics of the breakdown of the KH structures is not well elucidated by these experiments.

[6] Numerical and theoretical modeling studies do a very good job of studying the fine structure and physics of the evolution and breakdown of KH Instabilities. The importance of three-dimensional (3-D) simulations was implied by the hypothesis of *Davis and Peltier* [1979] that buoyancy-induced instabilities that form in the core of the KH vortex produce shear-aligned convective rolls perpendicular to the main KH billow structures. A 2-D simulation by *Klaassen and Peltier* [1985a] showed the evolution of KHs and also suggested that for flows with a Reynolds number on the order of 500, a convective instability existed, which should lead to the formation of convective rolls. Additional, partly 3-D, numerical simulations by *Klaassen and Peltier* [1985b, 1991] revealed the formation of secondary convective instabilities and their breakdown into turbulence. As computing power became greater, fully 3-D simulations occurred, allowing a more realistic look at the evolution of KHs in general, and the secondary instability in particular [*Caulfield and Peltier*, 1994; *Palmer et al.*, 1994; *Fritts et al.*, 1996; *Palmer et al.*, 1996; *Werne and Fritts.*, 1999; *Caulfield and Peltier*, 2000; *Peltier and Caulfield*, 2003]. However, the reality of these modeling results has only partially been tested by comparison with experiments [*Thorpe*, 1985]. How accurately modeling describes the real atmosphere is still an open question, and understanding KH evolution and breakdown in realistic flows will require new investigations [*Peltier and Caulfield*, 2003].

[7] A combination of airglow imaging and Na lidar data can test the accuracy of some of these models. Recently, a new atmospheric observatory has been established on Mt. Haleakala on Maui. The observatory includes airglow imagers, operating at both optical and IR wavelengths, and a Na wind/temperature lidar. During the night of 15 July 15 2002, the imager saw multiple structures, that when combined with the lidar data, were consistent with the presence of the KH primary billows predicted by models. The formation of perpendicular structures, which may be the secondary instabilities predicted by models, was observed for two of the KH primary billows. Both the primary and perpendicular features were seen to decay into chaotic structures. In the following sections the observations are described, and the results are compared with several numerical models.

2. Experimental Instrumentation and Technique
2.1. Near-IR Camera

[8] A near-infrared camera, previously located at the Starfire Optical Range [*Hecht et al.*, 2002], was located on Mt. Haleakala, Maui, in March 2002. This camera, which is briefly described in the work of *Hecht et al.*

[2002], combines a custom wide-angle lens with a 256 × 256 HgCdTe detector array to provide images over an ≈73 × 73 degree region of the sky. One hundred and twenty-eight pixels across the center are approximately equal to 40 degrees or 61 km at 85 km altitude. The detector is a NICMOS3 device developed by Rockwell Science Center and is identical to the devices by the same name that are currently operating on the Hubble Space Telescope. The array consists of four 128 × 128 quadrants, each with their own readout circuitry. Unfortunately, since the Starfire experiment, one 128 × 128 pixel quadrant has been lost.

[9] The collecting lens, which consists of 10 separate antireflection (AC)-coated elements, provides an f/5 telecentric output. The output is passed through a four-position filter wheel to select two OH Meinel airglow emission lines, the nearby continuum, and an open position. These photons are then passed into a cryogenic enclosure, where a six-element reimaging system (also antireflection coated and optimized for transmission between 1.2 and 1.8 μm) reduces the image size to the 1 cm dimension of the array. At the detector surface the optics are operating at f/1.3. Within the cryogenic camera cell is a broadband astronomical "H" filter (1.55–1.75 μm) that transmits the output of the external filter. This "H" filter is sandwiched with a custom blocking filter that moves the red edge to 1.70 μm and considerably reduces the thermal background. In order to facilitate remote observations for extended periods when no servicing is possible, the entire optics/detector train is cooled by a commercial cryocooler. The device uses the free expansion of gas (Joule-Thompson effect) to provide an essentially vibrationless cooling head.

[10] For this experiment a fixed open filter position was used, allowing a spectral range (1.55–1.7 μm) determined by the internal filters to be imaged. Because the OH meinel (4,2) band brightness is almost 100 kilo-Rayleighs (kRy) [see, e.g., *Krassovsky*, 1962], the signal to noise (S/N) for a 1 s integration gives a S/N in a pixel of about 200:1. Images were exposed for about 1.5 s, and images were obtained approximately every 3 s.

[11] Finally, we note that there is some geometric distortion in the images, especially near the edge of images in that straight lines appear somewhat curved. Stars moving across the image from east to west move in somewhat curved lines away from the center pixels. Thus in the following sections we will emphasize the alignments of those features which are closer to the center of the image.

2.2. Na Wind and Temperature Lidar

[12] Nearly simultaneous temperature and wind data were obtained from the University of Illinois Na wind/temperature lidar system [*Bills et al.*, 1991; *Gardner and Papen*, 1995] colocated at the AEOS facility. This facility, which includes a 3.67 m diameter fully steerable astronomical telescope, is operated by the Air Force Research Laboratory at the Air Force Maui Optical Station (AMOS) and is located on top of Mt. Haleakala (20.7 N, 156.3 W) on Maui.

[13] The lidar technique derives wind velocity and temperature by using the peak and two wing frequencies to probe the shape of the Na D2 absorption line, which are functions of wind (Doppler shift) and temperature (thermal broadening). This lidar system uses the AEOS

3.67 m telescope and thus can measure winds and temperatures at better than 1 km vertical resolution with a few minutes of integration time. For this work the lidar obtained densities every 24 m, but these are averaged and either the resultant 96 or 480 m bins are used.

[14] In normal operation mode the lidar takes profiles in one of five positions: zenith (Z), 30 degrees off zenith to the north (N), south (S), east (E), or west (W). Typically, these profiles are acquired in ZNEZSW sequence, and meridional or zonal winds are obtained by dividing the off-zenith line-of-sight wind by the sine of 30 degrees.

[15] Except where noted, all profiles are smoothed using a Hamming window with 1 km and 30 min full widths in altitude and in time and interpolated on a 15 min 100 m grid. The effective full width at half maximum of this approach is about 0.5 km and 15 min. The Hamming window is used because it smooths the profile somewhat better than a simple running mean. Smoothing over this time interval is accomplished by interpolating all profiles to the same altitude scale. Since all positions are used, this effectively provides results over a plus or minus 30 degree angle from the vertical. Some comparisons are also made using a 15 min Hamming window, with interpolated data every 7.5 min, although the differences in most cases are small. Finally, some of the individual profiles are used with points binned at 480 m intervals.

2.3. Model Analysis

[16] In the next section, some of the data are presented with respect to two quantities that can be related to the stability of the atmosphere, the Richardson number (R_i), and the potential temperature (θ).

[17] The stability of the atmosphere is typically quantified by the Richardson number (R_i), defined as

$$R_i = \frac{(g/T)(dT/dz + g/C_p)}{(S)^2},\qquad(1)$$

where g is the acceleration of gravity, T is the atmospheric temperature, C_p is the specific heat at constant pressure, g/C_p is the adiabatic lapse rate, S is the magnitude of the vertical shear of the horizontal wind, and z is altitude [*Richardson*, 1920; *Beer*, 1974; *Gossard and Hooke*, 1975]. The numerator is the square of the Brunt-Vaisala frequency. More formally, if we take the vector wind velocity $\mathbf{U}$ to be the vector sum of the meridional wind whose magnitude is $\mathbf{U}_y$ and the zonal wind, whose magnitude is $\mathbf{U}_x$, then S^2 is given by $(d\mathbf{U}_x/dz)^2 + (d\mathbf{U}_x/dz)^2$, where the wind is measured as a function of altitude, the derivatives become deltas, and the direction of the shear vector is just the vector difference of the winds at two different altitudes. Here we used a separation of 500 m in altitude. When R_i is less than zero owing to a temperature lapse rate which exceeds the adiabatic lapse rate, the atmosphere is considered to be convectively unstable. When R_i is between 0 and 0.25 owing to either the presence of a large wind shear or a combination of a moderate wind shear and a large but not superadiabatic temperature lapse rate, the atmosphere is considered to be dynamically unstable. Although the limit at 0.25 has not been rigorously shown to be valid and there is still some
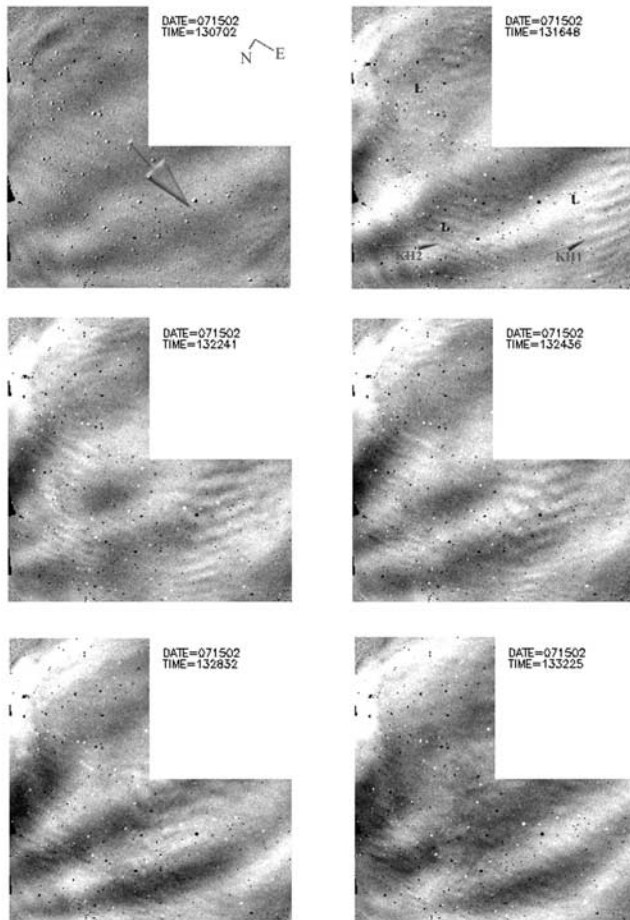
Figure 1. Six 256 × 256 images of the OH emission after flatfielding. The time and date are shown in the upper right quadrant. In the image at 1307:02 UT the large arrow points in the direction of motion of the wave whose crests are at the beginning and end of the arrow. The small arrows in the second image, at 1316:48 UT, point to the KH1 and KH2 billows. The letter "L" in bold indicates the position of the lidar when pointing toward the north, west and east from the vertical which is at the center of the image. The orientation of an image is shown in the first image. See text for additional discussion.

debate about this criterion, it remains a generally accepted indicator of a dynamical instability [*Werne and Fritts*, 1999; *Gossard and Hooke*, 1975; *Hines*, 1971].

[18] Potential temperature θ is defined as

$$\theta = T(p_0/p)^{R/C_p}, \qquad (2)$$

where T is the temperature measured at an altitude whose pressure is p, p_0 is a reference pressure level, R is the gas constant, and R/C_p is 0.286 for air. Lidar measurements provide temperature data as a function of altitude. The corresponding pressure can be calculated as follows using the lidar temperature data. A reference atmosphere can be used to provide a pressure at a given altitude several scale heights above the region of interest. Then the following formula given in the work of *Hauchecorne and Chanin*

[1980], and derived from combining hydrostatic balance and the ideal gas law, can be used to find the pressure at lower altitudes. This formula is

$$p_i = (p_u) \exp\left(\int_{z_i}^{z_u} (g/(RT))dz\right), \qquad (3)$$

where p_i is the pressure at altitude z_i, and p_u is the pressure at the upper boundary. The potential temperature generally increases with altitude. However, for regions where R_i is zero, the potential temperature is constant.

3. Results

3.1. Airglow Observations

3.1.1. Observations of KH Evolution Between 1300 and 1345 UT

[19] Figure 1 shows a sequence of six images, each one exposed for 1.5 s, taken between 1307 and 1332 UT on 15 July 15 2000. In each image, three 128 × 128 pixel quadrants are shown, with the bad quadrant being used to display the date and time of the exposure, and in the first image, the N and E directions. Each image has been normalized by dividing the raw image by the average of images taken between 1300 and 1305 UT, a normalization image. Before normalizing, owing mainly to the camera optics, the brightest part of each image is the center and the edges are dim, and thus it is difficult to see low contrast features. However, features present in the normalization image can show up as a fixed pattern in the normalized images. Thus it is important to show sequences of images and look for changes between images.

[20] The first image at 1307 UT is dominated by two phase fronts whose direction of motion is indicated by an arrow. Only faint small-scale structure is seen. Near the tip of the arrowhead one of many stars can be seen as a bright white circle with a small black section toward the lower left. The black portion, which shows up as a black dot in the other images, represents the position of the starfield in the flatfield image. The second image at 1316:48 UT shows the appearance of two sets of structures. Those labeled KH1 have phase fronts separated by about 7 km, assuming an altitude of 85 km, which move toward the NW in succeeding images. Those labeled KH2 have phase fronts separated by about 3.5 km, and they move toward the W in succeeding images. The KH1s appear to form phase fronts perpendicular to the main phase fronts by 1324 UT and seem to be dissipating in the last two images. The perpendicular phase fronts are separated by about the same distance as is the primary wave fronts. The KH2s do not appear to form additional structure. They fade but do not disappear by the last image. Visually, the last image at 1332 UT shows considerably more faint structure than the first one at 1307 UT.

[21] A better way to bring out the contrast in, and study the evolution of, faint moving structures is to apply the image difference approach used in many previous studies. In this approach, successive images are subtracted. This acts as a high pass filter, allowing the observation of any feature that changes and eliminating features fixed with respect to the time difference. No flatfielding is needed in this approach. If the time interval
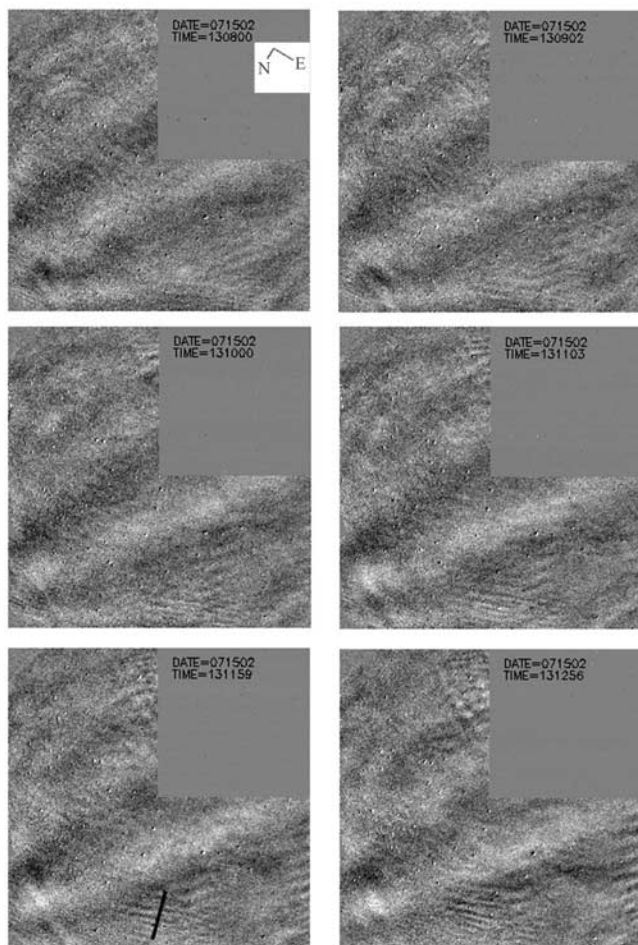
the additional bright spots that form and move with the primary KH1 phasefront appear to line up to form phasefronts that are approximately perpendicular to the primary KH1 phasefronts. These perpendicular phase fronts are clearly visible by 1322 UT. Because of the distortion of straight lines near the edge of the images, both primary and perpendicular phasefronts appear somewhat curved, but the perpendicular phasefronts close to the center portion of the image do appear to line up perpendicular to the primary phasefronts as shown in Figure 5.

[22] The motion of the KH1 structures, both primary and perpendicular, are toward the NW. The perpendicular structures appear to be fully formed by 1327 UT. Both primary and perpendicular structures appear to break up and dissipate, and they are considerably faded by 1336 UT. However, at 1336 UT, compared to the initial image at 1308 UT, considerable structure is visible that appears somewhat chaotic. This chaotic structure appears present until the last image available in this sequence at 1345 UT.
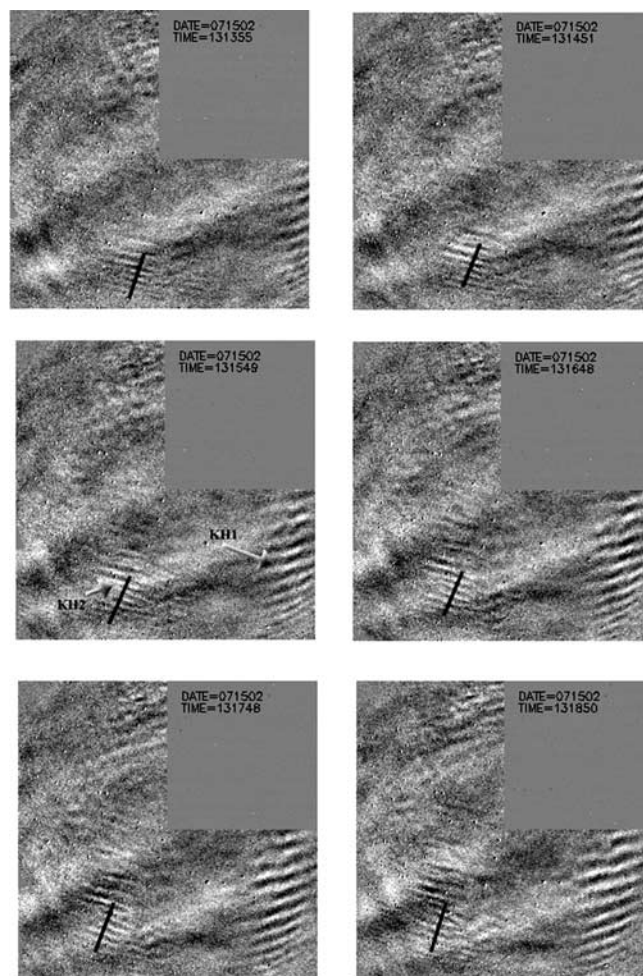

Figure 2. A sequence of six 1 min difference images separated by 1 min beginning at 1308 UT. The dark bold line in the image at 1311:59 UT is aligned perpendicular to the KH2 phasefronts. The following four figures complete the sequence which continues through 1336 UT. The orientation of an image is shown in the first image.

between the images used for differencing was equal to the time it takes for the bright features to travel one wavelength (one wave period), then the resultant difference image for a monochromatic wave would yield a zero signal. However, if the time difference is equal to one half of a wave period, then the signal level will appear to be both positive or negative. Here we picked 1 min as the time difference, which maximizes the contrast as this is approximately equal to half the wave period. Figures 2–6 show montages of images at 1 min intervals between 1308 and 1336 UT. In the first image at 1308 UT the same large wave structure is seen; evidently, its amplitude is changing within a minute time frame. By looking at the sequence of images, it can be determined that the KH1 (KH2) structures first appear about 1310 (1309) UT. The motion of the KH1 features is about 90 m/s toward the NW. A bright spot appears in one of the KH1 phase fronts at 1319 UT, and this may be the first indication of the subsequent formation of phase fronts that align themselves approximately perpendicular to the main phasefronts (see arrow in Figure 4). This and

Figure 3. Additional 1 min difference images. See Figure 2. The dark bold line in each image is aligned perpendicular to the KH2 phasefronts to allow the reader to see their progression. In the image at time 1315:49 UT the KH1 and KH2 phasefronts are labeled and pointed to by arrows to help guide the reader.
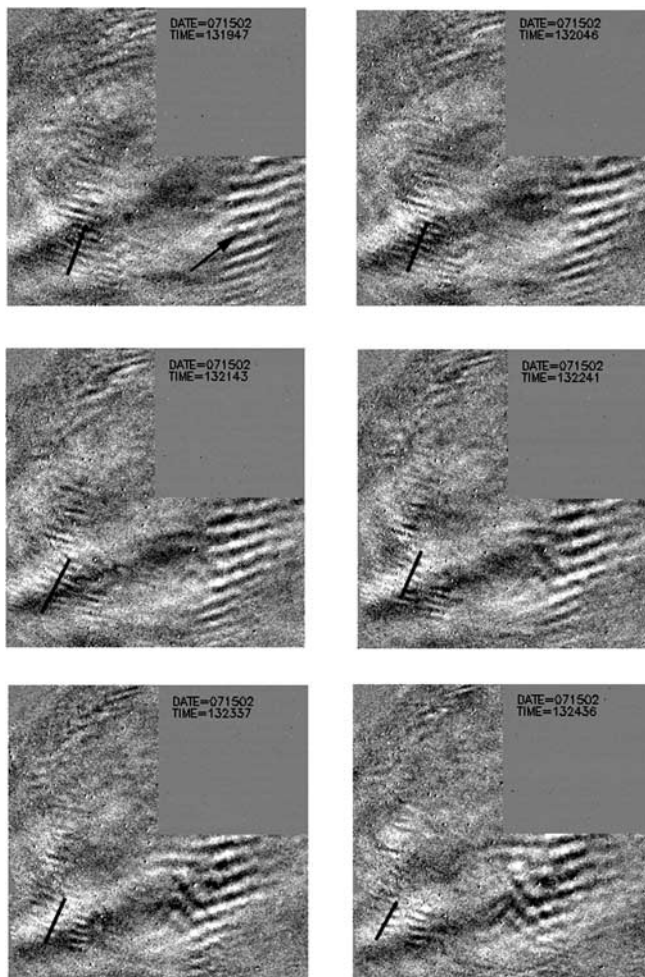
Figure 4. Additional 1 min difference images. See Figure 2. The dark bold line in the lower left-hand quadrant in each image is aligned perpendicular to the KH2 phasefronts to allow the reader to see their progression. For the image at 1319 UT an arrow points to the position of the bright spot referred to in the text.

[23] The KH2 structures appear to move toward the W, almost parallel to their phase fronts. They increase in brightness until about 1323 UT, when they begin to fade. No perpendicular structures form. They are still present at 1336 UT when they move outside the image. However, new features with the same KH2 alignment appear after 1330 UT and still persist at 1345 UT.

[24] Figures 7 and 8 show eight of these difference images with additional dark reference lines superimposed. The intensity along these reference lines are shown in Figure 9 and provide a measure of the strength and wavelength of the KH1 features. In these observations the nominal background is 2700 units, and thus the region of the billow peak would be 2800 if the billow amplitude is 100 in a raw image. Here no values are seen where the OH brightness decreases below 2700. Now in a difference image we subtract two raw images separated by 1 min, a time period chosen to maximize the wave-like appearance and during which the billows move one half a wavelength.

Thus one sees peak regions of amplitude 100 (2800 from one image minus 2700 of the image 1 min later) separated by regions of −100 amplitude (2700 minus 2800). Therefore the plots seen in Figure 9 appear to be wave-like.

[25] In these observations the motion of the KH1 features are such that after 1 min the motion of both the KH1 primary and perpendicular features have traveled about one half a wavelength. For the KH2 features, since they are moving nearly parallel to their phase fronts, there is effectively no increase or decrease in brightness produced by this differencing technique.

[26] For the KH1 features the line plot in Figure 9 at 1318 UT shows that they are separated by about 7 km (12 pixels). Each of the phase fronts has an amplitude of about 100–150 units. In fact, an examination of the raw flatfielded images indicates that the structure amplitudes are indeed this level above the background. The structures do not appear to be decreasing the emission below the average background level. Given that the background OH emission
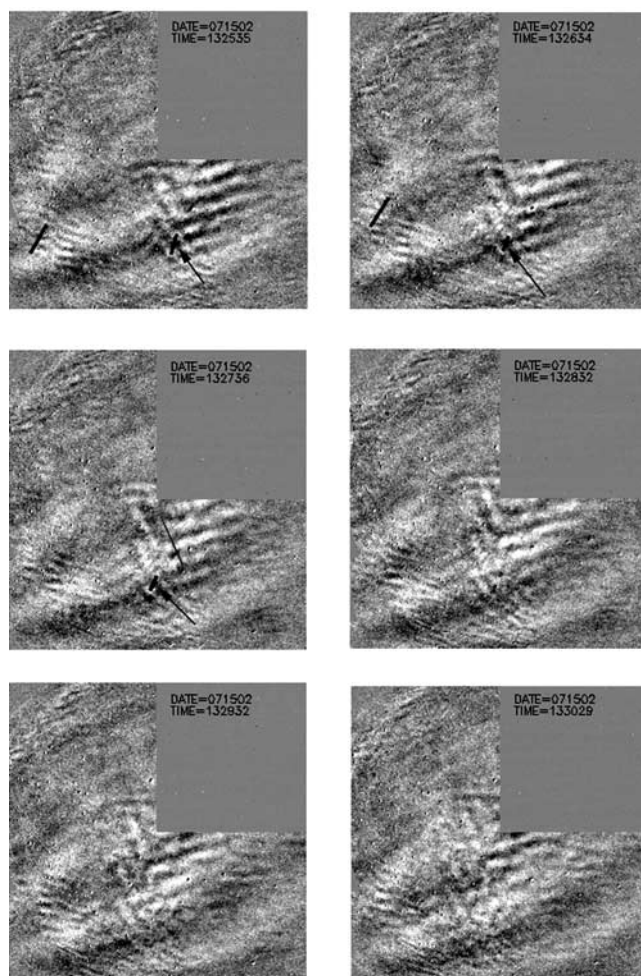

Figure 5. Additional 1 min difference images. See Figure 2. For the three images from 1325 to 1327 UT an arrow points to a short line we added on each image in the lower right quadrant. This line connects two bright spots which we associate with secondary instabilities. For the image at 1327 UT an additional long line was added in the lower right-hand quadrant to indicate a KH1 perpendicular phasefront.
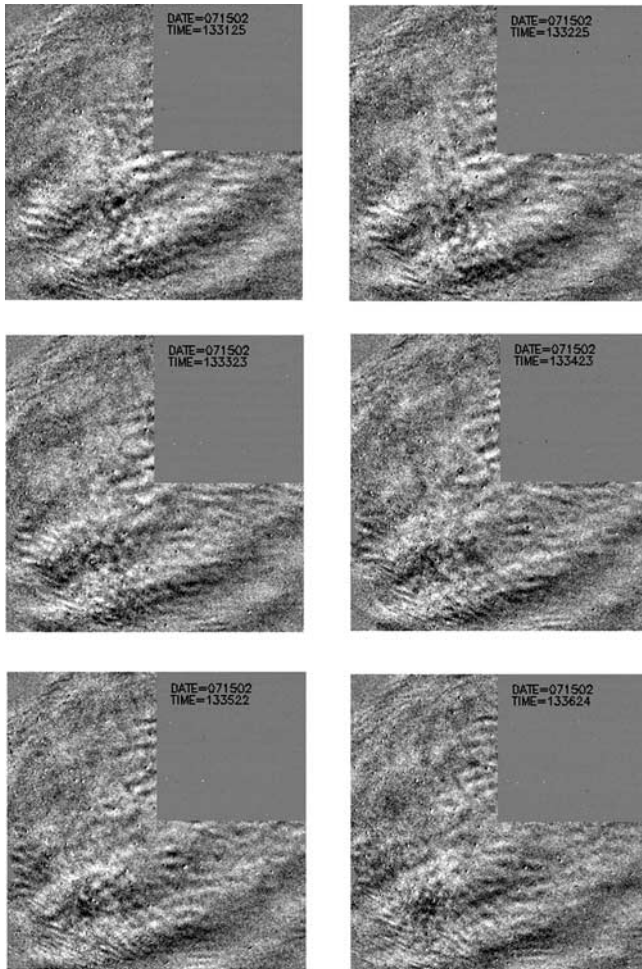
Figure 6. Additional 1 min difference images. See Figure 2.

lar phasefront based on the width and shape of the structures at 1326 UT. The perpendicular structures are about half as bright as the primary structures.

[28] The KH2 structures can be seen below pixel 100 on the cut at 1326 UT. The features are less than half as bright as the KH1 features and are separated by about 7 pixels or 4.3 km. Note that the lowest level associated with the KH2 structures is zero, suggesting that these structures produce a positive but not a negative perturbation on the OH brightness.

3.1.2. Observations of KH Evolution Between 1355 and 1420 UT

[29] The KH1 structures discussed above show perpendicular features occurring which are not seen in the KH2 structures. The formation of the perpendicular structures,
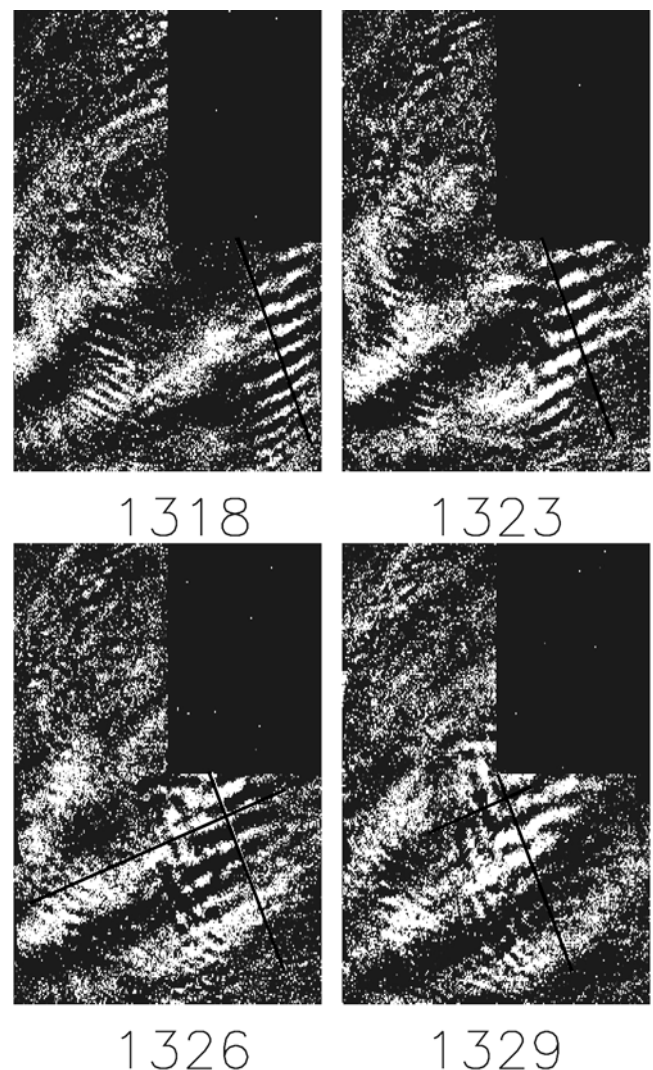

Figure 7. A series of four difference images chosen to show the motion and development of the KH1 billows. The series is continued in the next figure. The black line present on all the images is a cut through the KH1 billows. The magnitude of the OH emission through the cut is shown in Figure 9. At 1326 and 1329 UT, two other cuts are shown. They cut through the secondary instabilities and, at 1329 UT, through the KH2 billows.

is about 2700 units, the KH1 structures are perturbing the OH emission by about 3.7–5.5%. The structures weaken after 1329 UT but appear to be present in some organized fashion even at 1346 UT, although by that time they are no stronger than other features. The strength of these structures means that the local perturbation in OH brightness over a 1 km thick region is between 30 and 50%, depending on the thickness of the OH layer, which can be between 7 and 10 km [see, e.g., *Hecht et al.*, 1997]. However, temperature and density perturbations are probably less than 10% since Krassovsky's ratio of the OH brightness to OH temperature perturbations is on the order of 5 for short period short wavelength features [see, e.g., *Schubert et al.*, 1991]. Note though, that there is no specific model which calculates the Krassovsky's ratio of KH billows, so the use of the ratio derived for gravity waves is only approximate.

[27] To examine the perpendicular and KH2 features, two other reference line cuts at 1326 and 1329 UT are shown in Figure 10. The horizontal wavelength of the perpendicular features, which appear between pixel numbers 150 and 200, is about 7 km, which is very similar to the wavelength of the primary KH1 billows. At 1326 UT, before they are fully formed, they are somewhat broader than at 1329 UT. There is also some indication of fine structure in each perpendicu-
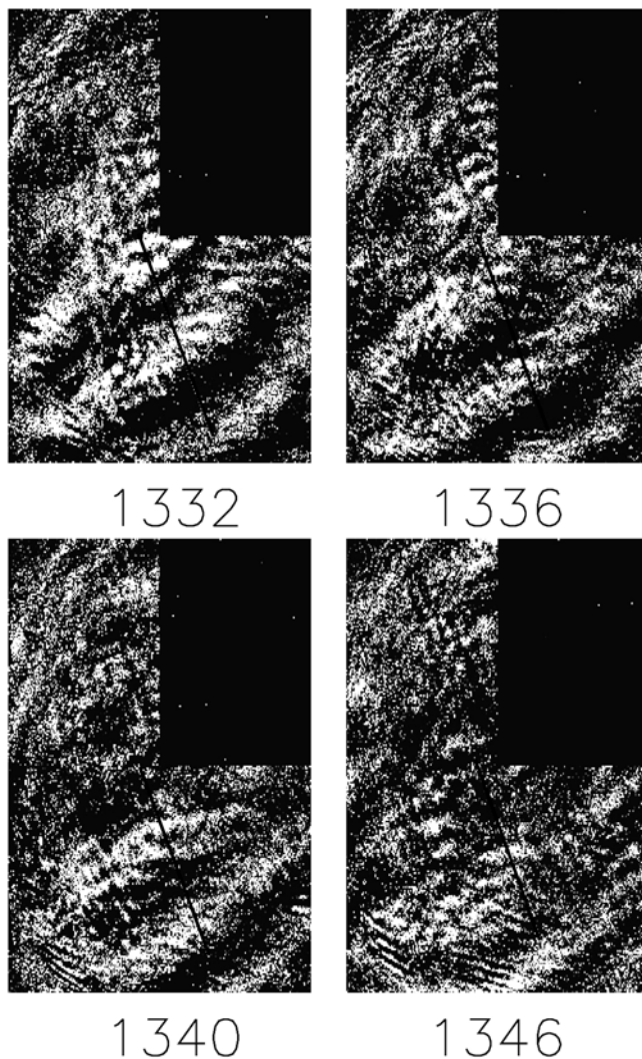
Figure 8. Additional 1 min difference images. See Figure 7.

however, are not unique. Figure 11 shows three additional 1 min difference images at 1357, 1404, and 1418 UT. Primary KH structures (KH3), very similar to the KH1 features, are seen blowing across the image. The horizontal wavelength at 11 km is somewhat larger while the amplitude of the perturbation at 2.5% is about half as strong. At 1404 UT, perpendicular structures are seen to form, as was found for the KH1 features. As before, the perpendicular structures appear as prominent bright spots on the primary crests which line up to form a phasefront approximately perpendicular to the primary KH3 phasefront. The perturbation of the OH brightness by the perpendicular structures is close to 0.5%, making them fainter with respect to the primaries than was found for the KH1s. Decay of these KH3 structures is well underway by 1418 UT. The life cycle of the KH3 features seems quite similar to the KH1s.

3.2. Lidar Temperature, Wind, and Na Density Observations

[30] Figure 12 shows contour plots of the Na density, the meridional and zonal winds, and the temperature obtained on 15 July 15 2002. The data here are the 1 hour smoothed Hamming window products where all data, regardless of look angle, are binned together for the temperature and wind profiles. The key feature here is the large wind shear that appears in the meridional component just above 85 km from 1300 UT onward. The contour plot indicates a negative, but not necessarily superadiabatic, temperature gradient between about 86 and 88 km. The magnitude is difficult to see on this plot, but an examination of individual profiles shows gradients at times around 1330 UT approaching the adiabatic lapse rate of near 9.5 K/km. The Na density shows an overturning feature beginning about 1330 UT between 85 and 87 km. An overturning feature is where transport of Na causes the vertical gradient of sodium density to reverse sign, with low density over high in the bottom side of the Na layer and the reverse in the top side. Na density is taken to be a quasi-tracer in the sense that the local changes in concentration of interest are primarily controlled by vertical advection. It has been observed in previous studies [Hecht et al., 1997, 2000] consistent with this one that regions where Na density appears to "overturn" are very closely associated with regions where potential temperature surfaces are overturned (i.e., where the temperature gradient is superadiabatic).

[31] In Figure 13 the lidar temperature and wind data are used to calculate R_i between 85 and 90 km, the region of the peak OH emission. The top panel uses the 1 hour Hamming data. The blue regions are where R_i is less than 1, the red regions are where R_i is less than 0.25, the nominal onset of a dynamical instability, the green regions are where R_i is less than 0.13, and the black regions are where R_i is less than 0, the nominal onset for a convective instability. The most striking feature is the large region of dynamical instability that begins at 1300 UT and continues for at least an hour. The altitudes where the atmosphere is unstable are between 85.5 and 87 km. Around 1330 UT a region of even lower R_i, due to a more negative temperature gradient, appears between 86 and 87 km. The unstable region as a whole appears to persist longer at the higher altitudes. Given the several degree uncertainty of individual profiles, averaging, either spatial or temporal, is needed to reduce the temperature uncertainty in order to determine if the temperature lapse rate is exceeding the adiabatic lapse rate, which is necessary for R_i to become less than zero. However, if such an instability occurs for only a short period, averaging, either temporal or spatial, can lessen the gradient so that R_i will appear to be greater than 0. The bottom panel uses the 15 min Hamming data. The general picture is similar, although the vertical extent and duration of the instability is less. However, both suggest that a convective instability might be occurring around 1330 UT, as suggested by the Na density data.

[32] This can be investigated more thoroughly by just using the potential temperature data, and Figure 14 shows plots of potential temperature and Na density versus altitude. Potential temperature nominally increases with altitude, as does Na density in the region below 90 km. For a region of convective instability where R_i is just zero, the potential temperature contours should appear vertical, while for superadiabatic lapse rates, where R_i is less than zero, the contours should appear to be overturned as described above. Just at 1330 UT the potential temperature does suggest a
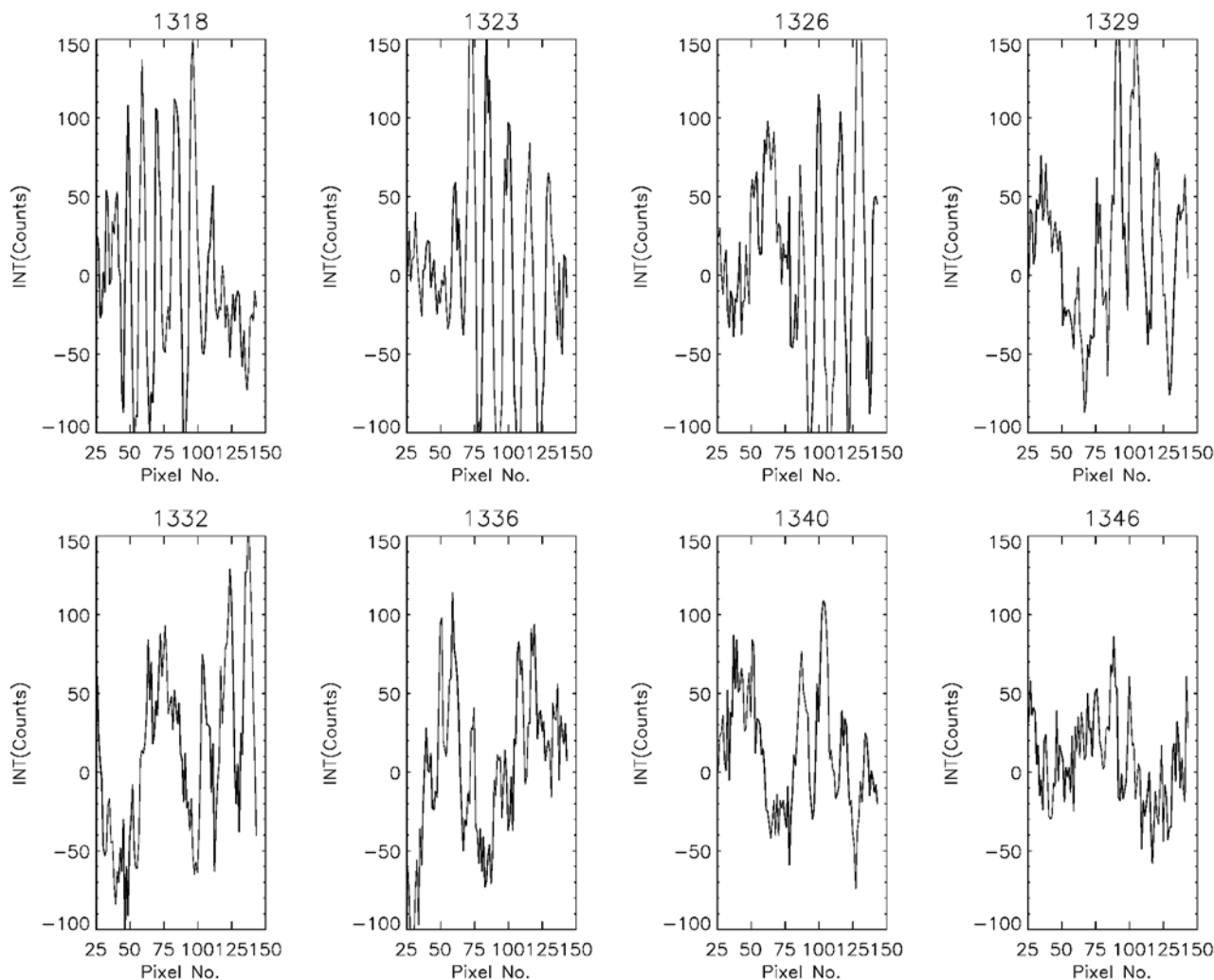
Figure 9. Eight plots of the magnitude of the OH difference emission versus position as represented by the horizontal pixel number.

nearly adiabatic lapse rate in the region between 86.5 and 87.5 km. This near adiabatic lapse rate continues for at least an hour. A comparison of the potential temperature plot with the Na density plot shows significant agreement in shape throughout the night, suggesting that the Na density is indeed a quasi-tracer, as suggested in previous studies [*Hecht et al.*, 1997, 2000]. Significant overturning occurs at 1330 UT which persists throughout the remainder of the night. Since Na density is measured with much more accuracy than is temperature or potential temperature, the Na density results are suggestive of a real convective instability occurring.

[33] The data above are all averaged data, so Figure 15 shows individual θ plots for three periods; at 1331:42 UT when the lidar was looking at 30 degrees off vertical to the west, 1333:24 UT when the lidar was looking overhead, and at 1335:10 UT when the lidar was looking 30 degrees off vertical to the north. For these plots, no Hamming window was used, and the actual data points every 480 m are shown. The dotted line is an average of the three profiles after the individual data were rebinned. In general, θ increases in altitude between 85 and 88 km. Any larger-scale feature
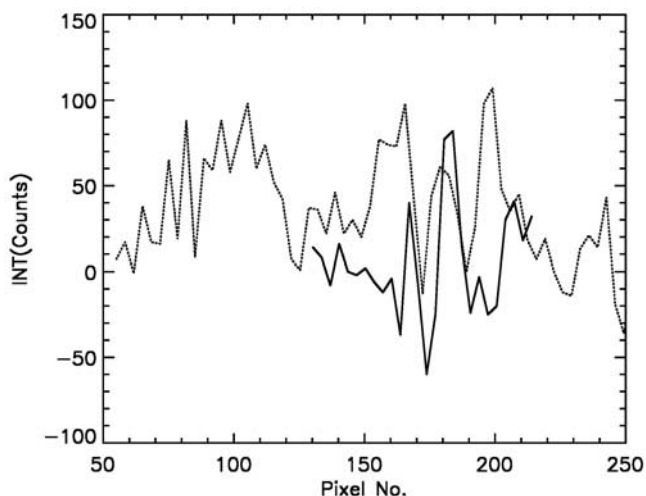

Figure 10. Same as Figure 9 but for the additional perpendicular cuts at 1326 UT (dotted line) and 1329 UT (solid line).
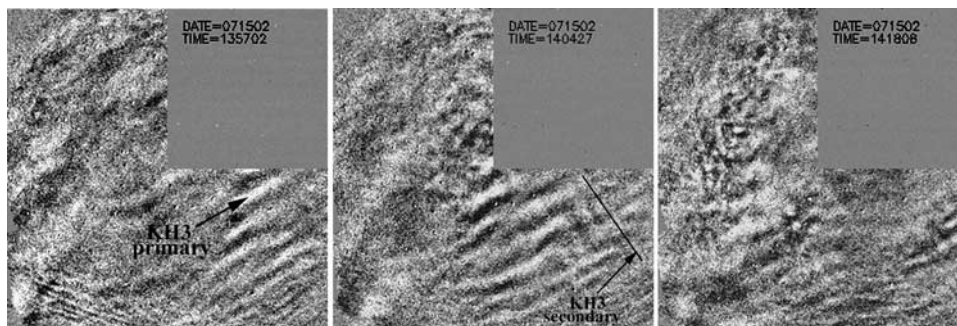
Figure 11. A sequence of OH difference images after 1356 UT on 15 July. (left) Appearance of primary KH3 structures. The arrow points to a crest. (middle) Appearance of secondary structures at 1404 UT. A line is drawn perpendicular to the primary KH3 structure parallel to a phasefront of the KH3 secondary. (right) Turbulence at 1418 UT.

might be expected to repeat on all three plots, although spatial differences could cause an individual plot to differ. Nevertheless, the negative gradient in one of the plots around 85.5 km could be due to noise in the temperature measurement. All three profiles, however, do show negative gradients between 86.5 and 87.5 km, suggesting a real convective instability occurs during this period. The dotted line suggests about a 500 m unstable region with a fractional overturning of 5K/215K or 2.3%. This is of the same order as the local density perturbation, which is inferred from the KH1 perpendicular structure observations. These data suggest that the perpendicular structures in the airglow

images are the convectively unstable secondary structures predicted by model simulations.

[34] Figure 16 shows a plot, using the 15 min Hamming data, of R_i, wind velocity, wind direction, and shear direction versus altitude at 1315 UT, when the KH1 structures began to appear on the images. The shear direction is calculated from the change of the horizontal wind vector with altitude. The R_i data show that the region of the dynamical instability extends from 85.5 to 87 km with minimum values of about 0.17. The shear is pointed from the NE to SW at least above 86 km, with the shear becoming more N to S closer to 85 km. Wind speeds are
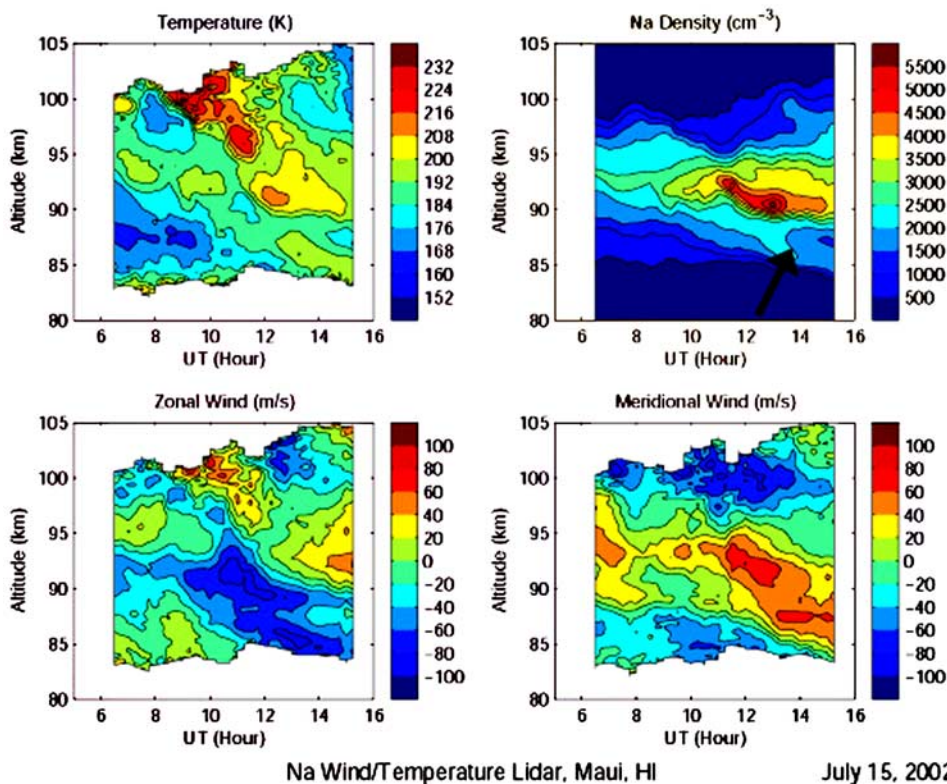
Figure 12. Four contour plots of the Na density, the meridional and zonal winds, and the temperature as measured by the lidar on 15 July. In the Na density panel the arrow points to the overturning feature described in the text.
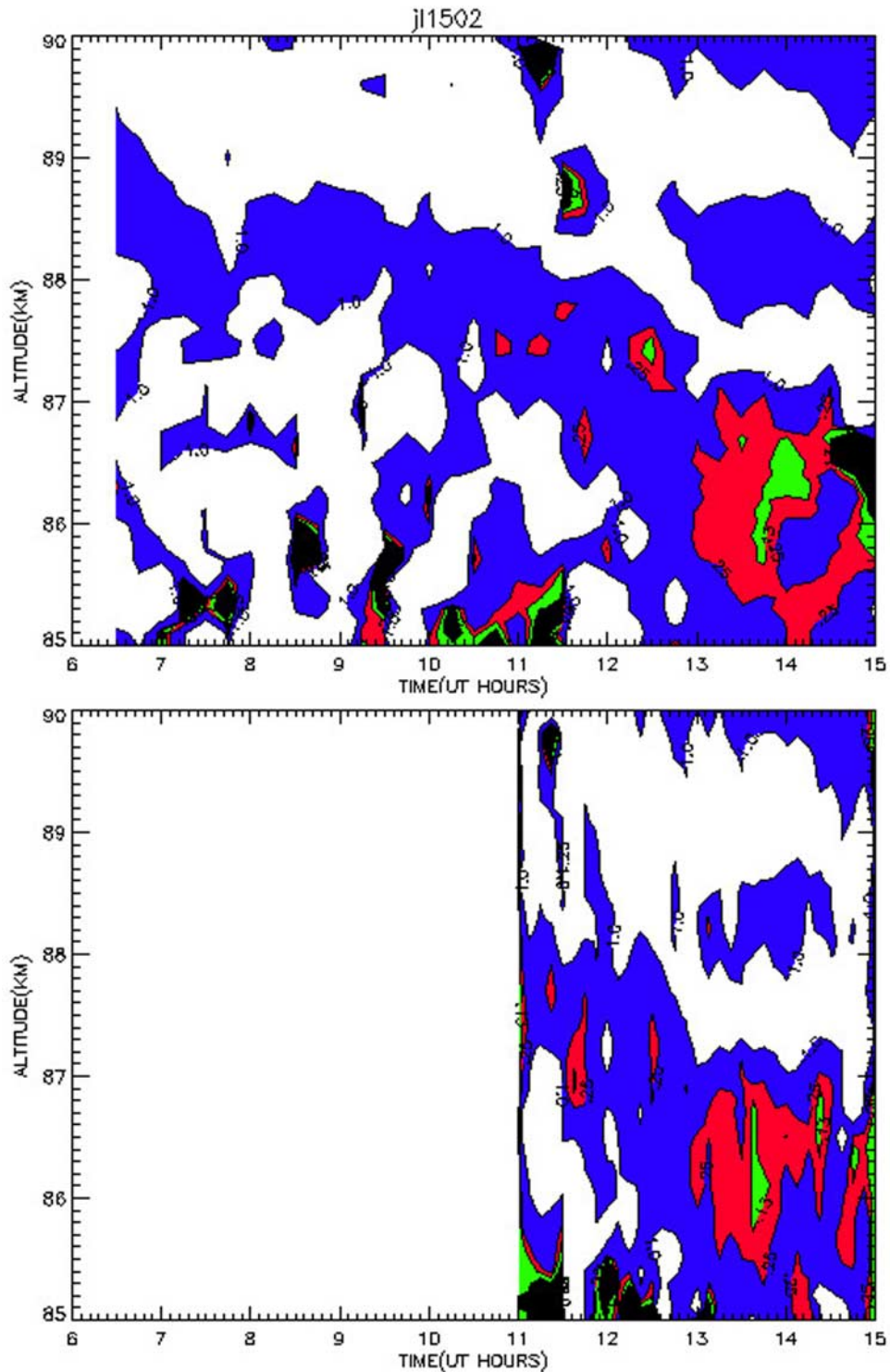
Figure 13. Two plots of R_i versus altitude and time. The bottom plot uses the 15 min Hamming window data, while the top plot uses the 1 hour Hamming window data. For the bottom plot, data are only shown after 1100 UT. The contours are marked with the value of R_i. White is when R_i is above 1, red is when R_i is between 0.25 and 0.13, green is when R_i is between 0.13 and 0.0, and black is when R_i is less than 0. Thus red and green regions are dynamically unstable and black regions are convectively unstable.
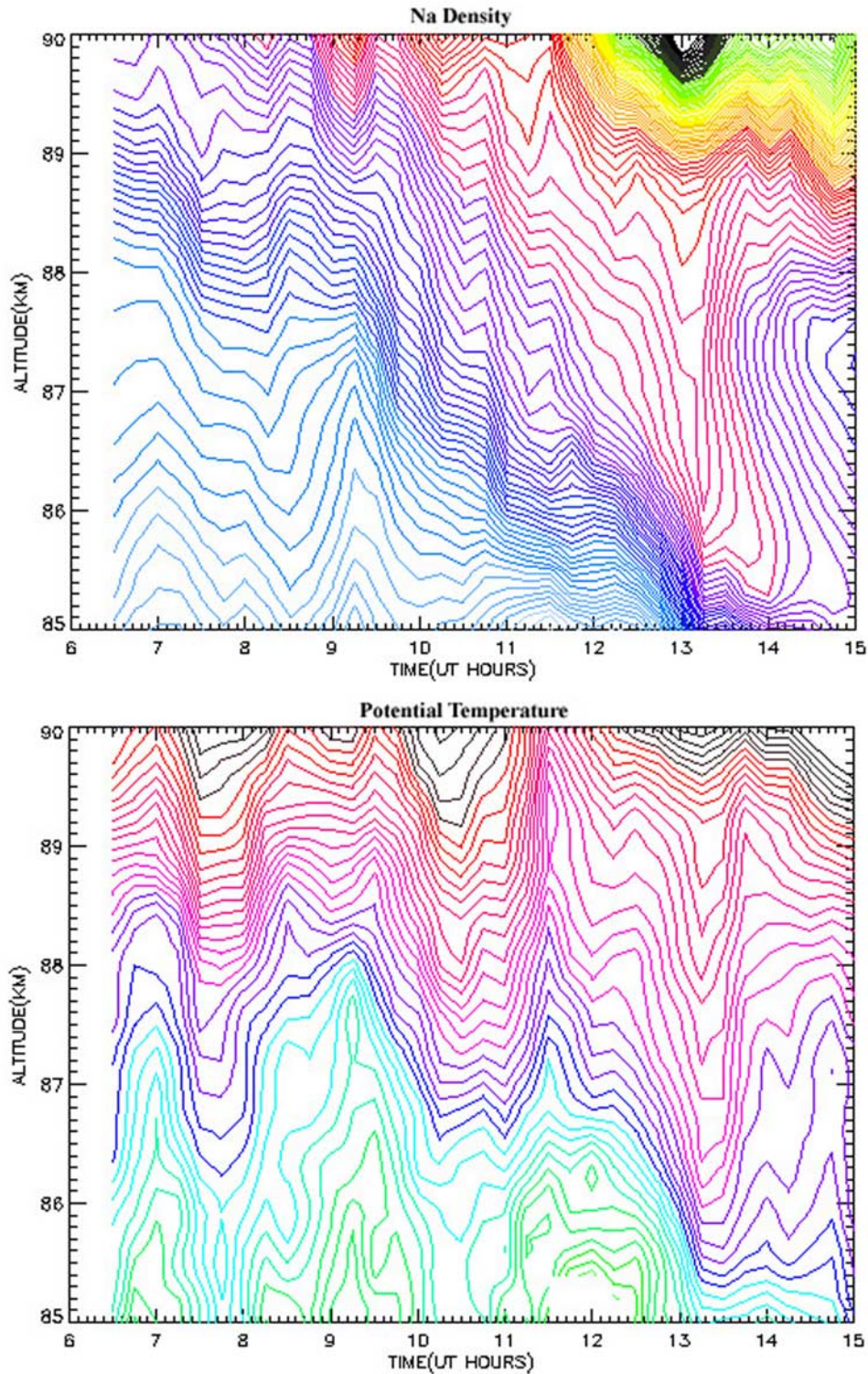
Figure 14. Two contour plots of (top) the Na density and (bottom) the potential temperature as a function of altitude and time. In general, the gradient is such that both parameters are increasing with altitude. However, there are regions where this is not the case. The most significant such region occurs between 86 and 87 km after 1300 UT where both the potential temperature and Na density are overturned. The colors and contour intervals are arbitrary and were chosen to highlight the region of interest.
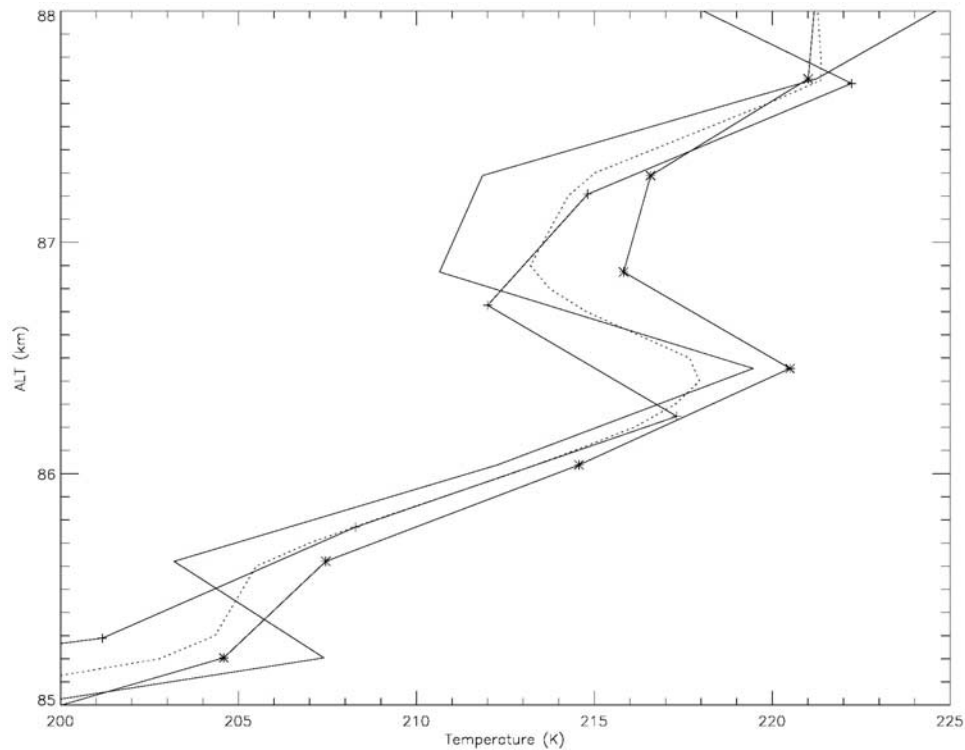
Figure 15. A plot of the potential temperature at 1331:42 UT (solid line with cross symbol), 1333:24 UT (solid line with plus symbol), and at 133510 UT (solid line). The lidar was looking 30 degrees off vertical to the west, overhead, and 30 degrees off vertical to the north during these times. The dotted line is an average of the three profiles after the individual data were rebinned.

Figure 16. Four plots versus altitude of R_i, the wind speed, the shear direction, and the wind direction. The zero direction is toward the north, with east displayed as positive from zero.

Figure 17. An image at 1322 UT of the OH difference emission. Lines are shown to represent the direction of the wind and the shear (within 180 degrees) as measured by the lidar at 85.9 km and at 1315 UT. The orientation of the KH2 phase fronts is also shown.

quite substantial, over 70 m/s. The wind direction is different than the shear direction, being more toward the W.
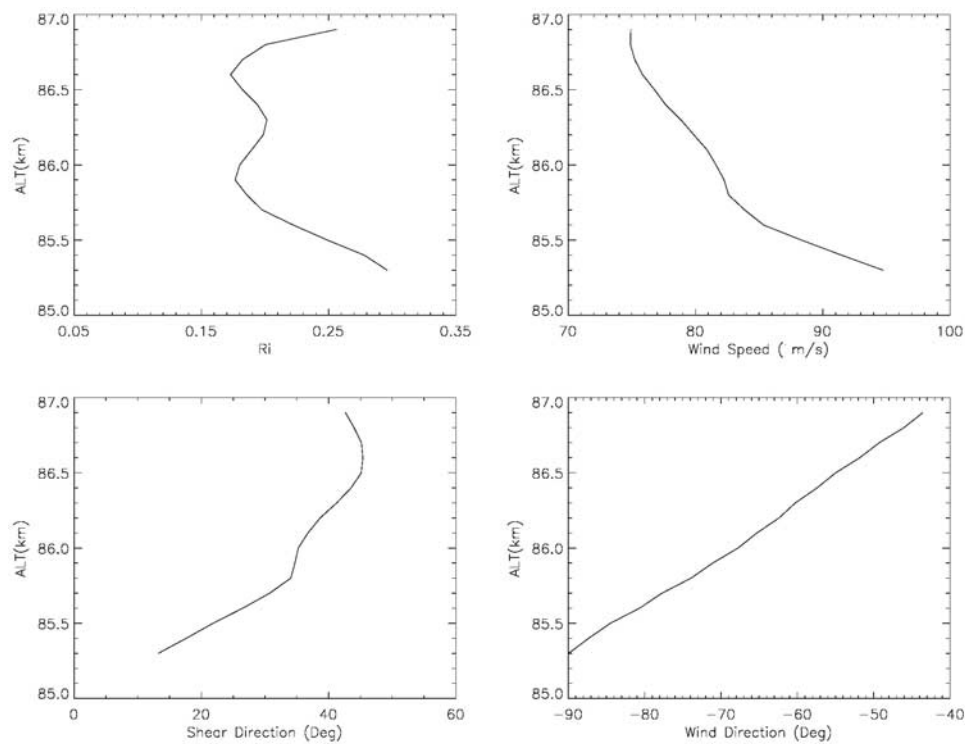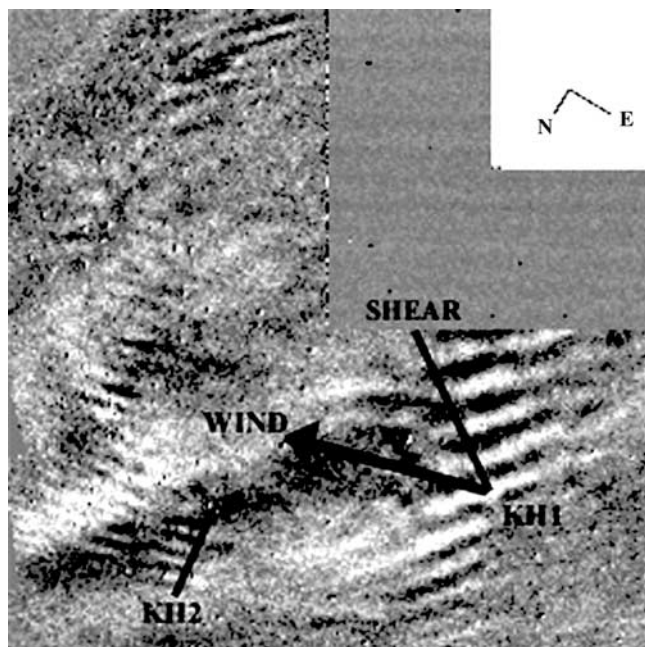
[35] In Figure 17 these velocity and shear vectors are overplotted with the KH1 features. On the basis of the direction of motion of the KH1 features, it is determined that the wind velocity at 85.9 km is the best match. The lidar wind speed is about 82 m/s, slightly below that of the KH1 features but within any error of both of those measurements. The corresponding shear vector appears to be perpendicular to the KH1 phase fronts, consistent with their being KH instabilities. The KH2 features are aligned differently as shown. However, the lidar data suggest that the shear vector is rotating toward that alignment at altitudes close to 85 km. However, at those altitudes, uncertainties in the calculation of R_i preclude a definite determination of the existence of an instability.

4. Discussion

[36] There are a number of numerical models that are potentially suitable for comparison with our data. Here we use four: (1) the *Klaassen and Peltier* [1985a, 1985b, 1991] 2-D models (hereinafter designated KP); (2) the fully 3-D models of *Fritts et al.* [1996] and *Palmer et al.* [1996] (hereinafter designated FP); (3) an updated version the FP model by *Hill et al.* [1999] and *Werne and Fritts* [1999] (hereinafter designated HW); and (4) the higher-resolution mostly 3-D simulations of *Caulfield and Peltier* [2000] and *Peltier and Caulfield* [2003] (hereinafter designated PC). The first three parameterize their models by R_i, which is taken as 0.05 in FP and HW and is variable in KP and also by the Reynolds number R_e, which is taken as 300–900 in

KP, 300 and 500 in FP, and 2000 in HW. The PC model is an updated use of the KP model but now including fully 3-D simulations. The value of R_e is taken as 750 and that of R_i as 0–0.125.

[37] The Reynolds number is given by

$$R_e = hU_m/\eta, \tag{4}$$

where following KP, h is taken as the half depth of the unstable layer. In KP and PC, U_m is half the magnitude of the velocity difference across the unstable layer. Since the features are seen to move with the wind, here U_m is calculated from the lidar wind data. The definitions of h and U in FP and HW are nearly the same. Classically (and in the FP, HW, PC, and KP models), η is given by the molecular kinematic viscosity which at these altitudes is 1–2 m²/s. However, at 86 km the kinematic viscosity is dominated by the eddy viscosity, which is highly variable. The eddy viscosity may be two orders of magnitude higher than the molecular kinematic viscosity, and here we assume a nominal value of 100 m²/s on the basis of the work of *Garcia and Solomon* [1985]. If the issue here was the transition from laminar flow to turbulence and the evolution of KH billows into a nonturbulent background, then the molecular kinematic viscosity would be appropriate. However, because this work is concerned with the formation and decay of KH billow structures in a background atmosphere that may be turbulent prior to the billow formation, and turbulence might play a role in the formation of billows and secondary instabilities, we consider the possible effects of turbulence when applying the theory. We acknowledge that the use of the models in this way is ad hoc and done advisedly. The unstable structures, however, are much larger than typical eddy sizes, which are on the order of 100 m or less. A complication though is that standard values of the eddy kinematic viscosity are spatial and temporal averages, while in a given instance, it may be quite variable over even narrow altitude regions [e.g., *Luebken*, 1997]. Nonetheless, the eddy viscosity formalism with its limitations should be appropriate in the spirit of a first approximation [e.g., *Beer*, 1974].

[38] To proceed, we take η to be a variable with three values of 100, 10, and 1 m²/s, which span the range of eddy to molecular kinematic viscosity. This will allow us to see to what extent the model results describe our observational data. The low value will allow us to test whether the models as formulated describe our results. The higher values will provide some idea of whether enhanced viscous effects can improve the observation to model agreement. It will require, however, more formal modeling studies in the future to fully investigate the effects of preexisting turbulence.

[39] For the KH1 features, U is taken as 30 m/s and h as 500 m, giving values of 150, 1500, and 15,000 for R_e assuming values η of 100, 10, and 1 m²/s, respectively. The lowest R_e value is derived assuming the nominal eddy diffusivity, while the highest R_e value would be valid for molecular kinematic viscosity.

[40] For the KH2 features, R_e is much less well known. It is known that for KH features in general, the separation of the phase fronts is about 8 times the depth of the instability layer [e.g., *Miles and Howard*, 1964; *Chandrasekhar*, 1981]. Thus we take h for KH2 to be about 250 m. U is

also poorly known, although the lidar data suggest values of between 10 and 30 m/s for the unstable regions between 84 and 85 km at and after 1300 UT. If we take U as 20 m/s, then R_e assumes values of 5, 50, and 500 for η of 100, 10, and 1 m^2/s, respectively.

[41] For the KP model results the evolution of KH billows is given in actual seconds as a function of R_e. In the FP model a characteristic time is given in terms of H/c, where H is the scale height and c is the speed of sound. For a temperature at 86 km of between 190 and 200 K, as measured by the lidar, this characteristic time unit is 21 s. In HW and in PC the characteristic time is given in terms of h/U, which for the KH1 billows is 17 s and for the KH2 billows is 12 s. In the following discussion we translate the characteristic times into actual seconds.

4.1. Lifetime of KH Versus Model

[42] The FP model results show billow formation beginning after about 1.5 min approaching maximum amplitude at around 6 min and reaching maximum amplitude at about 8 min. The collapse of the billows into turbulence begins after about 12 min and is complete by about 25 min. For the 500 R_e simulation, secondary instabilities begin to appear sometime after 9 min and are fully developed at around 11 min. While the billow collapse begins then, the secondary structures remain coherent until about 17 min. However, by 20 min the secondary structures no longer appear as distinct features. For an R_e of 300 the secondary instabilities do not appear in the potential temperature isosurfaces until about 15 min. Billow collapse is slower, and the collapsing structures appear more coherent and less turbulent than for the 500 R_e case. This can be seen by comparing time 56 (20.5 min) [see Palmer et al., 1996, Plate 1] with time 72 (26.4 min) [see Palmer et al., 1996, Plate 3].

[43] For the HW model and the KH1 features the timescales are similar. Maximum billow growth occurs at around 10 min. Between 4 and 8 min later (between 14 to 18 min), secondary instabilities appear, as evidenced by the transition to 3-D structure. By 29 min, these structures have collapsed, meaning the lifetime of the secondaries is around 10 min, similar to what was found by FP for the $R_e = 500$ case.

[44] The KP model shows a slightly longer time, between 3.5 and 7 min, for initial billow formation, but this depends on the detailed initial conditions of the mean flow chosen for the simulations. If 5 min is taken for the billows to first form, then at about 8–11 min they achieve maximum amplitude, after which the wave amplitude begins to oscillate. The FP model, however, suggests that some of the oscillation for the higher R_e cases (500 or greater) may be due to the 2-D nature of the KP analysis. KP also show that the maximum wave amplitude depends on R_i number with lower amplitudes for higher R_i numbers. For the 500 R_e case a superadiabatic region occurs in the billow core at around 9 min. This is the site of the secondary instability. By about 2 min later, at 11 min, the secondary instability achieves its maximum growth rate. By 13 min, the secondary instabilities have achieved their maximum amplitude, which has an amplification factor of about 20–30% of the primary KH billow. The growth rates for the secondary instabilities are much lower at an R_e of 300.

[45] For the PC model, which is only for an R_e number of 750, the timescales to achieve maximum billow amplitude is between 40 and 60 nondimensional time units or between 11 and 17 min for the KH1 billows and between 8 and 12 min for the KH2 billows. The secondary instabilities begin to form at this time rapidly (within a few minutes), achieving a significant amplitude. The lifetime of the secondaries is between approximately 20 and 30 min.

[46] These timescales compare very favorably with our data for the KH1 billows. R_i goes below 0.25 sometime around 1305 UT, and the images show billow formation occurring around 5 min later near 1310 UT. By 1315 UT, the billows reach near maximum amplitude. Thus the time for billows growth is consistent with all the models. The images show the first indication of perpendicular structure formation at 1319 UT, just about the time of maximum billow amplitude. The visible appearance of the perpendicular structures around 1322 UT indicates an increase in their growth rate. Maximum perpendicular structure amplitude is reached by 1327 UT, and both primary billows and perpendicular structures are considerably faded by 1336 UT. These timescales seem more consistent with the 300 rather than the 500 R_e simulations. The further agreement with the models continues to suggest that the perpendicular structures are indeed the predicted secondary instabilities. We note, however, that for the primary KH billow lifetime the agreement is somewhat better for the lower R_e simulations.

[47] Interestingly, the cross sections displayed in these various models (see, e.g., Hill et al. [1999, Figure 1] and discussions in the work of Caulfield and Peltier [2000] and Peltier and Caulfield [2003]) indicate that the secondary structures first appear in the outer core of the KH billows. This seems consistent with our observations of a brightening on the primary crests as a first indication of secondary formation.

4.2. Lifetime of Mesopause Versus Troposphere KH Billows

[48] Finally, it is worth mentioning that the KH billows observed in these data near the mesopause appear to last somewhat longer than the KH billows observed in the tropospheric radar observations of KH billows reported by Browning [1971] and Browning and Watkins [1970]. In those studies a majority lasted less than 15 min. Browning and Watkins [1970] provided data for one KH with a U_m of 8 m/s and an h of 200 m at approximately 6 km altitude where η would be a few times 10^{-5} m^2/s assuming molecular viscosity. The atmosphere at this altitude would thus have a very high R_e number. The KH lifetime was about 15 min.

[49] These lifetimes are comparable to or somewhat less than what was observed in the current study near the mesopause. In general, it would be expected that the lifetime near the mesopause might be somewhat less than in the middle to upper troposphere since the mesopause temperatures are somewhat lower, and the characteristic time from the models, H/c, scales as the square root of the temperature. The observations here that show a somewhat longer lifetime than expected from this scaling argument may be related to the actual value of the eddy diffusivity near 85 km. Nevertheless, both studies taken together indicate that KH instabilities can form both at low

and at high altitudes over a range of atmospheric temperatures and diffusivities.

4.3. Appearance of Secondary Instabilities Versus Model Rayleigh Number

[50] *Woods* [1969] suggested that there is a critical R_e of around 300, below which the KH billows do not undergo a turbulent collapse. The KP and FP models both confirm this approximate criterion. Another way of looking at this was discussed by *Davis and Peltier* [1979], who suggested that a buoyancy-induced instability formed in the core of the wave. In an analogy with the Rayleigh-Bernard thermal convection problem, they suggested that a calculation of the Rayleigh number would reveal if the core region became unstable. The Rayleigh number measures the relative importance of buoyancy effects and diffusion, and for Rayleigh-Bernard experiments, values that exceed around 1700 are considered unstable [*Lesieur*, 1997]. *Klaassen and Peltier* [1985b] define a local Rayleigh number associated with a superadiabatic region as

$$Ra = \frac{(g\Delta\theta\delta^3)}{(T\kappa\eta)}, \qquad (5)$$

where δ is defined as the vertical distance at which $d\theta/dz$ vanishes, and κ is the thermal diffusivity. The ratio of η/κ is known as the Prandtl number, which for air is 0.73 [*Fritts et al.* 1996]. However, the turbulent Prandtl number, which relates eddy viscosity and eddy diffusivity, may be somewhat less, on the order of 0.5 [*Lesieur*, 1997]. For equation (5) the turbulent Prandtl number will be used. The Rayleigh number depends on the cube of the depth of the superadiabatic region and inversely on the square of the eddy diffusion. As before, we will use a variety of values for η in making this analysis.

[51] For the KH1 billows, Ra is $(9.8)(.023)(500^3)/$ $((2.)(100)(100))$ or 1408 for an eddy diffusivity of 100 m^2/s. This is just around the critical Ra number. The Ra number is even greater for smaller eddy diffusivities. However, given the uncertainties in η discussed at the beginning of this section and in δ, this only shows the plausibility that the KH1 billows are convectively unstable. We note that the perpendicular structures associated with the KH3 features are weaker than those associated with the KH1 features. However, the eddy diffusion is probably greater for the period of the KH3 features, perhaps making the KH3 structures only marginally convectively unstable.

[52] The KH2 billows are only half the wavelength of the KH1 billows, suggesting an unstable layer on the order of a factor of two smaller. Given the dependence of Ra on δ, this suggests that Ra is well below the critical value, providing the eddy diffusivity is above about 30 m^2/s. Thus diffusion effects dominate, and as is observed, convective unstable secondary instabilities would not be expected to form.

[53] This has important implications for the production of turbulence by the ripple structures observed in airglow images. It implies that if their horizontal wavelengths are below about 7 km, the production of turbulence and the resultant increase in eddy diffusion could be minimal for small-scale KH billows like the ones observed in this study.

4.4. Horizontal Wavelength of Observed Perpendicular Structures Versus Model Predictions for Secondary Instabilities

[54] While the evolution times for the KH1 structures agree reasonably well with the model predictions for the primary KH billows and secondary instability structures, especially for the 300 R_e model, the horizontal wavelength of the perpendicular structures is much larger than what is shown in any of models for the secondary instabilities. At R_e of 300 the ratio of the primary to secondary in the models is about 4, with the ratio increasing for increasing R_e. Moreover, the KP model bandwidth of the secondary instability wavelengths is much broader than for the primary instability which also seems inconsistent with the data.

[55] While it is possible that what we are observing as perpendicular structures are artifacts and they are actually chance superpositions of primary KH billow structures originating at different altitudes, the following considerations strongly suggest these features are indeed the secondary instabilities predicted by models.

[56] 1. They are seen on two separate occasions associated with primary structures (KH1 and KH3) billows. Thus a chance superposition is unlikely to be the cause of these observations on two separate occasions.

[57] 2. They appear to form at the crests of the billows.

[58] 3. They move with the primary structures. This means they are moving with the same wind speed as the primary structures. However, the wind is rotating with height, and thus it is likely that they are occurring at the same altitude as the primary billows. The lidar winds indicate that there is no other region within the airglow emission region, which extends from about 82 to about 92 km, where the winds are the same as at 86 km. While the lidar winds as shown in Figure 12 only extend to just below 85 km, there are meteor winds at about 3 km vertical resolution available for this night (S. Franke, private communication, 2004). These show no evidence of any additional shear below 85 km, although the shear region around 86 km is visible, and indicates that the winds below 85 km are indeed blowing in a different direction than is seen at 86 km. In addition, these data when combined with the lidar data indicate that the only region with a 1 km or so thick dynamically unstable region during this period occurred between 86 and 87 km. The only way an unstable region could exist below 85 km and be consistent with the available data is if there was a nearly adiabatic lapse present below 85 km. However, even then the winds would be blowing in the wrong direction.

[59] 4. In simulations convectively unstable, secondary structures form perpendicular to the primary KH structures, and here in our observations the perpendicular structures appear when the atmosphere at the altitude of the primary KH structures goes convectively unstable, strongly suggesting that these are indeed a secondary instability. Taken together, all the above arguments suggest that the perpendicular structures are convectively unstable secondary instabilities. If the perpendicular structures are indeed secondary instabilities, there may be a way to reconcile differences between the observations and the model predictions. (1) KP

models the dependence of the ratio of the scales of the primary and secondary instabilities as a function of R_e, and as R_e decreases to the critical value of 220, below which no secondary features form, the ratio also decreases. Between R_e values of 220 and 300 the ratio would approach 1, as is observed. Given the uncertainty in the inferred value of R_e, this could be the simplest explanation. However, the secondary instability horizontal wavelength bandwidth would still be broad. (2) KP also discuss the R_i dependence of the wavelength of the secondary instability. While there is some indication that at higher values (close to 0.25) the wavelength of the secondaries would increase, it does not appear that the R_i dependence alone is large enough to account for our observations. (3) KP also identified a mode for the secondary instability that resides in the central core of the primary billows. This mode, at least for R_i of 0.12 and below, has a narrow bandwidth and larger wavelength than the modes that reside in the outer core and that normally dominate the secondary instability. However, the wavelength of this mode is still too short to account for our observations.

[60] It is tempting to consider (1) as the solution. In that case the eddy diffusivity for the KH1 structures would be near 50 m^2/s (close to nominal). For the KH2 features, any value over molecular would produce a low R_e number. However, this implies that at least at the altitude of the KH1 features the atmosphere is already turbulent.

[61] It is also necessary to consider how OH images might see the secondary instabilities. The imager is sensitive to the column emission of OH airglow which extends from about 82 to 92 km. Thus an image is more sensitive to perturbations concentrated in the vertical at one portion of the billows rather than spread out over the whole billow. The cross sections displayed in these various models (see, e.g., *Hill et al.* [1999, Figure 1], discussions in the work of *Caulfield and Peltier* [2000], and *Peltier and Caulfield* [2003]) indicate that the largest amplitude secondary structures first appear in the outer core of the KH billows. However, there is some indication as indicated in the work of *Caulfield and Peltier* [2000, Figure 7] and *Klaassen and Peltier* [1991, Figure 15] that the modes with longer wavelengths (only twice the wavelength of the primary in those examples) may have their energy concentrated in the central core and more in the vertical than the shorter wavelength modes where the energy is spread over the entire core. Thus OH images may be preferentially more responsive to the longer wavelength modes. This also seems consistent with our observations of a brightening on the primary billow crests as a first indication of secondary formation.

[62] To summarize, the observations support and fail to support the identification of the perpendicular structures with the predicted secondary instabilities. Supporting the identification are (1) the lidar data which show that a convective instability does exist, (2) the image and lidar data which strongly suggest that the perpendicular structures form in association with this instability, and (3) the image data which show that the perpendicular structures move with the KH billows. The main contradiction with this identification are the image data which show that the wavelengths of the perpendicular structures are too long to be consistent with the values for the secondary instabilities predicted by current theory. Also it should be noted that the structures are

perhaps not always perfectly perpendicular to the main phasefronts. Although the models show the secondary instabilities to be perpendicular, the significance of the small deviation is unclear. We note that there is a remote possibility that we are seeing the chance superposition of two wave packets at different altitudes. However, as we describe above, this is not supported by the available data.

[63] Thus there is a need to reconcile the differences between observations and theory. The differences might be explained through a proper accounting of preexisting turbulence. However, with existing theory this must be done in an ad hoc fashion, and as suggested earlier, a more satisfactory explanation will require additional detailed modeling to investigate how Kelvin-Helmholtz billows and the associated secondary instabilities evolve in realistic flow conditions where the atmosphere may already be turbulent. In addition, these results need to be coupled with an analysis of how secondary instabilities would perturb the OH emission. If the perpendicular structures are secondary instabilities, the observations indicate a detailed theory is lacking for how these structures are generated for conditions near the mesopause.

4.5. Appearance of Turbulence and Persistence of Overturning

[64] The airglow observations indicate that turbulence persists after the collapse of the billows for at least 15 min. The potential temperature data show unstable conditions until about 1430 UT, and the Na data suggest overturning continuing until at least 1500 UT. The earlier simulations of KP and FP span about one half hour or less. Recently, *Werne and Fritts* [1999] performed a simulation at an R_e of 2000 but which spanned several hours. Turbulence begins after about 1000 s and continues significantly until about 3600 s. Some evidence of turbulence is still present though at 6000 s. *Werne and Fritts* [1999] assert that turbulence should end when R_i is greater than 0.25. Our results for this observation are contradictory. The potential temperature data are in agreement with this assertion as the measured R_i becomes greater than 0.25 around 1430 UT. The Na overturning data disagree; however, it is not clear whether the persistence of an overturning reflects continuing instability or merely the fact that once the atmosphere becomes well-mixed, it takes a considerable amount of time to become unmixed. Image data do exist between 1400 and 1500 UT, and they appear to show an atmosphere closer to what was seen at 1300 UT than at 1336 UT, in agreement with *Werne and Fritts* [1999].

5. Conclusions

[65] The main results of this study are as follows.

[66] 1. OH airglow image data show the evolution and breakdown of three different sets of KH primary billows. These primary billows are seen as ripple structures in the OH images, which form when R_i is below 0.25, are blown with the wind near 86 km, and have phasefronts aligned perpendicular to the wind shear vector near 86 km. Taken together, these data provide the best evidence to date that some of the ripples are indeed due to KH instabilities.

[67] 2. The timescales for the life cycle of the primary KHs agree well with models.

[68] 3. Phasefronts which are approximately perpendicular to the primary KH billows are observed to form at a time when the atmosphere goes convectively unstable. This and their association on two separate occasions with the primary KH billows suggest that these are convectively unstable secondaries. They were observed to form and decay as predicted by models (with one exception).

[69] 4. The Rayleigh and Reynolds numbers that are needed to be consistent with the model prediction of the formation of convectively unstable secondary billows suggest that the background kinematic viscosity needs to be taken as an eddy kinematic viscosity with a value on the order of 100 m^2/s rather than a molecular kinematic viscosity whose value is closer to 1 m^2/s.

[70] 5. The wavelength of the perpendicular structures was longer than is generally predicted for the secondary instabilities, although this may be a consequence of the eddy kinematic viscosity of the atmosphere at the time of their formation. However, resolution of this difference and the ad hoc increase in kinematic viscosity suggested above underscores the need for additional numerical modeling to determine how KH billows evolve in an already turbulent background atmosphere.

[71] 6. Secondary instability formation was not seen for very small-scale ripple features. This suggests that such small-scale ripples seen in OH airglow image data may not produce much turbulent mixing of atmospheric constituents.

[72] Finally, while in general the agreement with the model predictions is good, there is one aspect to which appropriate models have not been applied. Our observations show that the KHs occur over a limited region of the images; if x is the direction of the primary KH wave number, then in the models the wave number in the y direction is zero. The KH billows in the OH images, however, span only a limited region in the y direction. They form in patches of limited spatial extent. This should be addressed in more detailed modeling.

References

Beer, T. (1974), *Atmospheric Waves*, 300 pp., John Wiley, Hoboken, N. J.

Bills, R. E., C. S. Gardner, and C. Y. She (1991), Narrow band lidar technique for sodium temperature and Doppler wind observations of the upper atmosphere, *Opt. Eng.*, 30, 13–21.

Browning, K. A. (1971), Structure of the atmosphere in the vicinity of large-amplitude Kelvin-Helmholtz billows, *Q. J. R. Meteorol. Soc.*, 97, 283–299.

Browning, K. A., and C. D. Watkins (1970), Observations of clear air turbulence by high power radar, *Nature*, 227, 260–263.

Caulfield, C. P., and W. R. Peltier (1994), Three dimensionalization of the stratified mixing layer, *Phys. Fluids*, 6, 3803–3805.

Caulfield, C. P., and W. R. Peltier (2000), The anatomy of the mixing transition in homogeneous and stratified free shear layers, *J. Fluid Mech.*, 413, 1–47.

Chandrasekhar, S. (1981), *Hydrodynamic and Hydromagnetic Stability*, 652 pp., Dover, Mineola, N. Y.

Davis, P. A., and W. R. Peltier (1979), Some characteristics of the Kelvin-Helmholtz and resonant overreflection modes of shear flow instability and their interaction through vortex pairing, *J. Atmos Sci.*, 36, 2394–2412.

Fritts, D. C., T. L. Palmer, O. Andreassen, and I. Lie (1996), Evolution and breakdown of Kelvin-Helmholtz billows in stratified compressible flows. part I: Comparison of two- and three-dimensional flows, *J. Atmos. Sci.*, 53, 3173–3191.

Garcia, R. R., and S. Solomon (1985), The effect of breaking gravity waves on the dynamics and chemical composition of the mesosphere and lower thermosphere, *J. Geophys. Res.*, 90, 3850–3868.

Gardner, C. S., and G. C. Papen (1995), Mesospheric Na wind/temperature lidar, *Rev. Laser Eng.*, 23, 131–134.

Gossard, E. E., and W. H. Hooke (1975), *Waves in the Atmosphere, Atmospheric Infrasound and Gravity Waves—Their Generation and Propagation*, 456 pp., Elsevier Sci., New York.

Hauchecorne, A., and M.-L. Chanin (1980), Density and temperature profiles obtained by lidar between 35 and 70 km, *Geophys. Res. Lett.*, 7, 565–568.

Hauritz, B. (1964), Comments on wave forms in noctilucent clouds, *Geophys. Inst. Sci. Rep. UGAR 160*, Univ. of Alaska, Fairbanks.

Hecht, J. H., S. K. R. Howat, R. L. Walterscheid, and J. R. Isler (1995), Observations of spectra of brightness fluctuations of the OH Meinel nightglow during ALOHA 93, *Geophys. Res. Lett.*, 22, 2873–2876.

Hecht, J. H., R. L. Walterscheid, D. C. Fritts, J. R. Isler, D. C. Senft, C. S. Gardner, and S. J. Franke (1997), Wave breaking signatures in OH airglow and sodium densities and temperatures: 1. Airglow imaging, Na lidar, and MF radar observations, *J. Geophys. Res.*, 102, 6655–6668.

Hecht, J. H., C. Fricke-Begemann, R. L. Walterscheid, and J. Höffner (2000), Observations of the breakdown of an atmospheric gravity wave near the cold summer mesopause at 54N, *Geophys. Res. Lett.*, 27, 879–882.

Hecht, J. H., R. L. Walterscheid, M. P. Hickey, and S. J. Franke (2001a), Climatology and modeling of quasi-monochromatic atmospheric gravity waves observed over Urbana, Illinois, *J. Geophys. Res.*, 106, 5181–5195.

Hecht, J. H., R. L. Walterscheid, and R. A. Vincent (2001b), Airglow observations of dynamical (wind shear-induced) instabilities over Adelaide, Australia, associated with atmospheric gravity waves, *J. Geophys. Res.*, 106, 28,189–28,197.

Hecht, J. H., R. L. Walterscheid, M. P. Hickey, R. J. Rudy, and A. Z. Liu (2002), An observation of a fast external atmospheric acoustic-gravity wave, *J. Geophys. Res.*, 107(D20), 4444, doi:10.1029/2001JD001438.

Hill, R. J., D. E. Gibson-Wilde, J. A. Werne, and D. C. Fritts (1999), Turbulence-induced fluctuations in ionization and application to PMSE, *Earth Planets Space*, 51, 499–513.

Hines, C. O. (1971), Generalization of the Richardson criterion for the onset of atmospheric turbulence, *Q. J. R. Meteorol. Soc.*, 97, 429–439.

Klaassen, G. P., and W. R. Peltier (1985a), The evolution of finite amplitude Kelvin-Helmholtz billows in two spatial dimensions, *J. Atmos. Sci.*, 42, 1321–1339.

Klaassen, G. P., and W. R. Peltier (1985b), The onset of turbulence in finite amplitude Kelvin-Helmholtz billows, *J. Fluid Mech.*, 155, 1–35.

Klaassen, G. P., and W. R. Peltier (1991), The influence of stratification on secondary instability in free shear layers, *J. Fluid Mech.*, 227, 71–106.

Krassovsky, V. I. (1962), Atlas of the airglow spectrum 3000–12400 Å, *Planet. Space Sci.*, 9, 883–915.

Lesieur, M. (1997), *Turbulence in Fluids*, 515 pp., Kluwer Acad., Norwell, Mass.

Lloyd, K. H., C. H. Low, and R. A. Vincent (1973), Turbulence, billows, and gravity waves in a high shear region of the upper atmosphere, *Planet. Space Sci.*, 21, 653–661.

Luebken, F.-J. (1997), Seasonal variations of turbulent energy dissipation rates at high latitudes as determined by in situ measurements of neutral density fluctuations, *J. Geophys. Res.*, 102, 13,441–13,456.

Miles, J. W., and L. N. Howard (1964), Note on a heterogeneous shear flow, *J. Fluid Mech.*, 20, 331–336.

Moreels, G., and M. Herse (1977), Photographic evidence of waves around the 85 km level, *Planet. Space Sci.*, 25, 265–273.

Nakamura, T., A. Higashikawa, T. Tsuda, and Y. Matsushita (1999), Seasonal variations of gravity wave structures in OH airglow with a CCD imager at Shigaraki, *Earth Planets Space*, 51, 897–906.

Orlanski, I., and K. Bryan (1969), Formation of the thermocline step structure by large-amplitude internal gravity waves, *J. Geophys. Res.*, 74, 6975–6983.

Palmer, T. L., D. C. Fritts, O. Andreassen, and I. Lie (1994), Three dimensional Kelvin-Helmholtz billows in stratified compressible flow, *Geophys. Res. Lett.*, 21, 2287–2290.

Palmer, T. L., D. C. Fritts, and O. Andreassen (1996), Evolution and breakdown of Kelvin-Helmholtz billows in stratified compressible flows. part II: Instability structure, evolution, and energetics, *J. Atmos Sci.*, 53, 3192–3212.

Peltier, W. R., and C. P. Caulfield (2003), Mixing efficiency in stratified shear flows, *Annu. Rev. Fluid Mech.*, 35, 135, doi:10.1146/annurev.fluid.35.101101.161144.

Peterson, A. W. (1979), Airglow events visible to the naked eye, *Appl. Opt.*, *18*, 3390.

Peterson, A. W., and L. M. Kieffaber (1973), Infrared photography of OH airglow structures, *Nature*, *242*, 321–322.

Richardson, L. F. (1920), The supply of energy from and to atmospheric eddies, *Proc. R. Soc. A*, *67*, 354–373.

Schubert, G., M. P. Hickey, and R. L. Walterscheid (1991), Gravity wave-driven fluctuations in OH nightglow from an extended dissipative emission region, *J. Geophys. Res.*, *96*, 13,869–13,880.

Scorer, R. S. (1969), The supply of energy from and to atmospheric eddies, *Radio Sci.*, *4*, 1299–1307.

Smith, S. M., M. Mendillo, J. Baumgardner, and R. R. Clark (2000), Mesospheric gravity wave imaging at a subauroral site: First results from Millstone Hill, *J. Geophys. Res.*, *105*, 27,119–27,130.

Swenson, G. R., M. J. Taylor, P. J. Espy, C. S. Gardner, and X. Tao (1995), ALOHA-93 measurements of intrinsic gravity wave characteristics using the airborne airglow imager and ground-based Na wind/temperature lidar, *Geophys. Res. Lett.*, *22*, 2841–2844.

Taylor, M. J., and M. A. Hapgood (1990), On the origin of ripple-type wave structure in the OH airglow emission, *Planet. Space Sci.*, *38*, 1421–1430.

Taylor, M. J., and M. J. Hill (1991), Near infrared imaging of hydroxyl wave structure over an ocean site at low latitudes, *Geophys. Res. Lett.*, *18*, 1333–1336.

Taylor, M. J., M. B. Bishop, and V. Taylor (1995), All-sky measurements of short period gravity waves imaged in the OI (557.7 nm), Na (589.2 nm) and near infrared OH and O2 (0,1) nightglow emissions during the ALOHA-93 campaign, *Geophys. Res. Lett.*, *22*, 2833–2836.

Taylor, M. J., W. R. Pendleton Jr., S. Clark, H. Takahashi, D. Gobbi, and R. A. Goldberg (1997), Image measurements of short-period gravity waves at equatorial latitudes, *J. Geophys. Res.*, *102*, 26,283–26,299.

Thorpe, S. A. (1968), A method of producing shear in a stratified flow, *J. Fluid Mech.*, *32*, 693–704.

Thorpe, S. A. (1973), Experiments on instability and turbulence in a stratified shear flow, *J. Fluid Mech.*, *61*, 731–751.

Thorpe, S. A. (1985), Laboratory observations of secondary structures in Kelvin-Helmholtz billows and consequences for ocean mixing, *Geophys. Astrophys. Fluid Dyn.*, *34*, 175–199.

Thorpe, S. A. (1987), Transitional phenomena and the development of turbulence in stratified flows: A review, *J. Geophys. Res.*, *92*, 5231–5248.

Walterscheid, R. L., J. H. Hecht, R. A. Vincent, I. M. Reid, J. Woithe, and M. P. Hickey (1999), Analysis and interpretation of airglow and radar observations of quasi-monochromatic gravity waves in the upper mesosphere and lower thermosphere over Adelaide, Australia (35°S, 138°E), *J. Atmos. Sol. Terr. Phys.*, *61*, 461–468.

Werne, J., and D. C. Fritts (1999), Stratified shear turbulence: Evolution and statistics, *Geophys. Res. Lett.*, *26*, 439–442.

Woods, J. D. (1969), On Richardson's number as a criterion for laminar-turbulent transition in the ocean and atmosphere, *Radio Sci.*, *4*, 1289–1298.

————————

J. H. Hecht, R. J. Rudy, and R. L. Walterscheid, Space Science Applications Laboratory, Aerospace Corporation, M2-259, P.O. Box 92957, Los Angeles, CA 90009, USA. (james.hecht@aero.org; richard.rudy@aero.org; richard.walterscheid@aero.org)

A. Z. Liu, Department of Electrical and Computer Engineering, University of Illinois, 308 C.S.L., 1308 W. Main Street, Urbana, IL 61801, USA. (liuzr@uiuc.edu)